PCCP

Single- and multi-photon-induced ultraviolet excitation and photodissociation of CH3I probed by coincident ion momentum imaging

Journal:	*Physical Chemistry Chemical Physics*
Manuscript ID	CP-ART-01-2023-000498.R1
Article Type:	Paper
Date Submitted by the Author:	14-Mar-2023
Complete List of Authors:	Ziaee, Farzaneh; Kansas State University, Physics Borne, Kurtis; Kansas State University, Physics Forbes, Ruaridh ; SLAC, PULSE Institute Kanka Raju, P.; Kansas State University, Department of Physics; DIAT (DU) Malakar, Yubaraj; Kansas State University, Department of Physics Kaderiya, Balram; Kansas State University, Department of Physics Severt, Travis; Kansas State University, Physics Department Ben-Itzhak, Itzik; Kansas State University, Physics Rudenko, Artem; Kansas State University, Department of Physics Rolles, Daniel; Kansas State University, Department of Physics

Single- and multi-photon-induced ultraviolet excitation and photodissociation of CH_3I probed by coincident ion momentum imaging

Farzaneh Ziaee [a], Kurtis Borne [a], Ruaridh Forbes [b], Kanaka Raju P. [a,c], Yubaraj Malakar [a], Balram Kaderiya [a], Travis Severt [a], Itzik Ben-Itzhak [a], Artem Rudenko [a, +], and Daniel Rolles [a, *]

[a] J. R. Macdonald Laboratory, Department of Physics, Kansas State University, Manhattan, KS 66506, USA

[b] SLAC National Accelerator Laboratory, Menlo Park, CA 94025, USA

[c] School of Quantum Technology, DIAT (DU), Pune, Maharashtra, India 411025

[+] rudenko@phys.ksu.edu [*] rolles@phys.ksu.edu

Abstract

The UV-induced photodissociation dynamics of iodomethane (CH_3I) in its *A*-band are investigated by time-resolved coincident ion momentum imaging using strong-field ionization as a probe. The delay-dependent kinetic energy distribution of the photofragments resulting from double ionization of the molecule maps the cleavage of the carbon-iodine bond and shows how the existence of a potential well in the di-cationic potential energy surfaces shapes the observed distribution at small pump-probe delays. Furthermore, the competition between single- and multi-photon excitation and ionization of the molecule is studied as a function of the intensity of the UV-pump laser pulse. Two-photon excitation to Rydberg states is identified by tracking the transformation of the delay-dependent singly-charged iodomethane yield from a pure Gaussian distribution at low intensity to a Gaussian with an exponentially decaying tail at higher intensities. Dissociative ionization induced by absorption of three UV photons is resolved as an additional delay-dependent feature in the kinetic energy of the fragment ions detected in coincidence.

***Keywords*:** UV-induced photodissociation, strong-field ionization, Coulomb explosion imaging, coincident ion momentum imaging, femtosecond dynamics

1. Introduction

For many decades, iodomethane (CH_3I) has served as one of the most popular model systems for studying light-induced dynamics of polyatomic molecules [1-50]. The reasons that make it particularly attractive include its importance in environmental science [51, 52], its relative simplicity (and, thus, accessibility for theory), the availability of extensive sets of spectroscopic data [4, 5, 13, 53, 54], and the rich variety of photochemical phenomena that are observed in this molecule. In particular, CH_3I photodissociation in its lowest-lying excited states, known as the *A*-band, represents a prominent example of a rather simple system passing through a conical intersection (CI) between two potential energy surfaces (PES) [29, 42, 48]. The *A*-band of iodomethane results from the excitation of a non-bonding 5*p* valence electron of the iodine atom to the lowest anti-bonding molecular orbital. This absorption band, centered at 260 nm, comprises three dipole-allowed transitions to low-lying excited states, which, following Mulliken notation [53], are labeled as $^1Q_1$, $^3Q_0$, and $^3Q_1$. The photoabsorption cross section is dominated by a parallel transition to the $^3Q_0$ state, resulting in C-I bond cleavage and the dissociation of the neutral molecule into the ground-state CH_3 radical and spin-orbit excited iodine atom $I^*(^2P_{1/2})$ [3, 11, 12, 17, 53]. During the dissociation, a fraction of the excited-state population is transferred to the $^1Q_1$ state via a non-adiabatic crossing between the $^3Q_0$ and $^1Q_1$, producing a CH_3 radical and a ground-state iodine atom $I(^2P_{3/2})$, as sketched in Fig. 1(a). The branching ratio between $I^*(^2P_{1/2})$ and $I(^2P_{3/2})$ depends on the exact excitation wavelength and has been reported to be 0.70 and 0.81 for 266 and 248 nm, respectively [3,11]. Close to the maximum of the *A*-band absorption cross section, the direct transitions to the $^1Q_1$ and $^3Q_1$ states are perpendicular and weaker, contributing less than 2% to the total absorption spectrum [11]. However, recent measurements show that different dynamics occur on the red and blue sides of the absorption band, most likely due to changes in the excitation cross sections of the accessible $^3Q_0$ and $^1Q_1$ states [20, 21, 43, 44, 47].

Despite decades of studies, the photodissociation of CH_3I continues to attract experimental and theoretical attention as a prototype for both naturally occurring [29, 42, 48] and light-induced [26, 42] conical intersections. Some of the more recent experimental studies include various time-domain measurement schemes such as transient absorption [29, 31, 48], time-resolved photoelectron [40, 43, 44, 47] and photoion [37, 40] spectroscopy, as well as (non-

coincident) Coulomb explosion imaging (CEI) [38, 39, 42]. In particular, a combined experimental and theoretical study [42], which employed intense near-infrared (NIR) probe pulses and velocity map imaging for ion detection, focused on potential advantages of the CEI approach for direct imaging of the nuclear molecular wave packet in the vicinity of a conical intersection, and on the role of the potential minimum of the di-cationic PES in the formation of the CEI patterns. In the present work, we show that *coincident* CEI combined with an improved time resolution (<45 fs vs 180 fs in Ref. [42]) can bring additional insights into the *A*-band photodissociation dynamics of CH_3I.

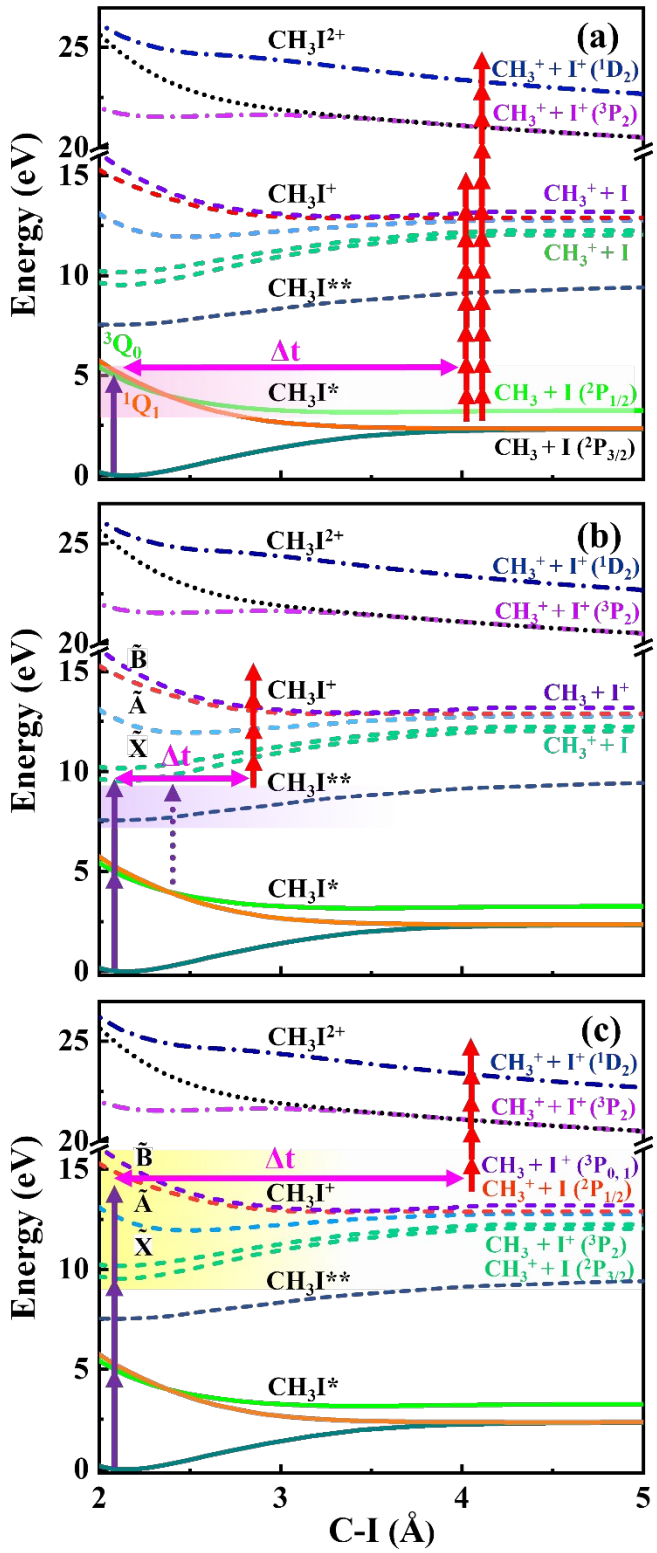

Figure 1: UV-excitation and NIR-ionization schemes on the relevant electronic states of CH_3I (neutral and ionic PECs adapted from Refs. [14, 23, 24, 35]). For reference, the purely Coulombic di-cationic potential is shown as a black dotted line. (a) Single-UV-photon excitation into the CH_3I A-band followed by NIR multi-photon ionization to various mono-cationic or di-cationic states. (b) Two-UV-photon excitation to CH_3I Rydberg states by either a direct transition or through intermediate neutral excited states (possibly with some

dynamics on the intermediate state, as indicated by the dotted blue arrow) followed by NIR multi-photon ionization. (c) Three-UV-photon ionization followed by NIR multi-photon ionization.

More specifically, this paper has three primary objectives. First, we focus on mapping the *A*-band dissociation via double ionization by a 25-fs, 800-nm NIR-probe pulse and coincident detection of the resulting CH_3^+ and I^+ fragments. Here, we observe a direct signature of the potential well in the di-cationic PES near the Franck-Condon region predicted by Corrales *et al*. [42]. Second, by analyzing the delay-dependent yields and kinetic energies (KE) of the reaction products at different intensities of the UV-pump pulse, we identify the dynamics driven by the absorption of one, two, and three UV photons. Such separation of single- or multi-photon-induced reaction pathways often plays an important role in the interpretation of time-resolved photochemistry experiments [18, 45]. Third, by analyzing the delay-dependent data for low-energy I^+ and CH_3^+ ions produced with a neutral partner, we discuss the possible influence of light-induced conical intersections [26] on the outcome of such UV-pump – NIR-probe measurements at short delays.

2. Experimental methods

A schematic of the optical setup, described in more detail in a previous publication [55], and the coincidence ion momentum imaging system is shown in Fig. 2(a). Briefly, the experiments utilize a Ti:Sapphire chirped-pulse amplification (CPA) laser system providing femtosecond near-infrared (NIR) laser pulses at a repetition rate of 10 kHz. The laser produces 23-fs [full width at half maximum (FWHM) in intensity] laser pulses with a central wavelength of 790 nm and pulse energy of up to 1.8 mJ. The linearly polarized output of the laser is split into two arms by an 80:20 beam splitter. The smaller fraction of the beam remains at the fundamental wavelength and is used as the probe pulse for strong-field ionization. The dominant fraction is frequency tripled using a pair of beta-barium-borate (β-BBO) crystals (150-μm and 20-μm thick, respectively) to generate the UV-pump pulse with a central wavelength of 263 nm, 7 nm bandwidth (FWHM in intensity), and up to 16 μJ pulse energy. A home-built calcium fluoride double-pass prism compressor [55] is used to compensate for the dispersion caused by transmissive optical elements in the beam path, which would otherwise lead to significant temporal broadening due to the large bandwidth associated with the pump pulse. The pump pulse is characterized by spectrally-resolved cross-correlation measurements with the NIR-probe

pulses using difference frequency generation (DFG). The DFG measurements show that the UV pulse is compressed to approximately 38 fs (FWHM) [55], based on independent frequency-resolved optical gating (FROG) measurement of the NIR pulse duration, which yields 23 fs (FWHM). A computer-controlled delay stage in the probe-beam path provides a variable time-delay between the two pulses that is scanned from -300 to 3000 fs with a step size of 10 fs.

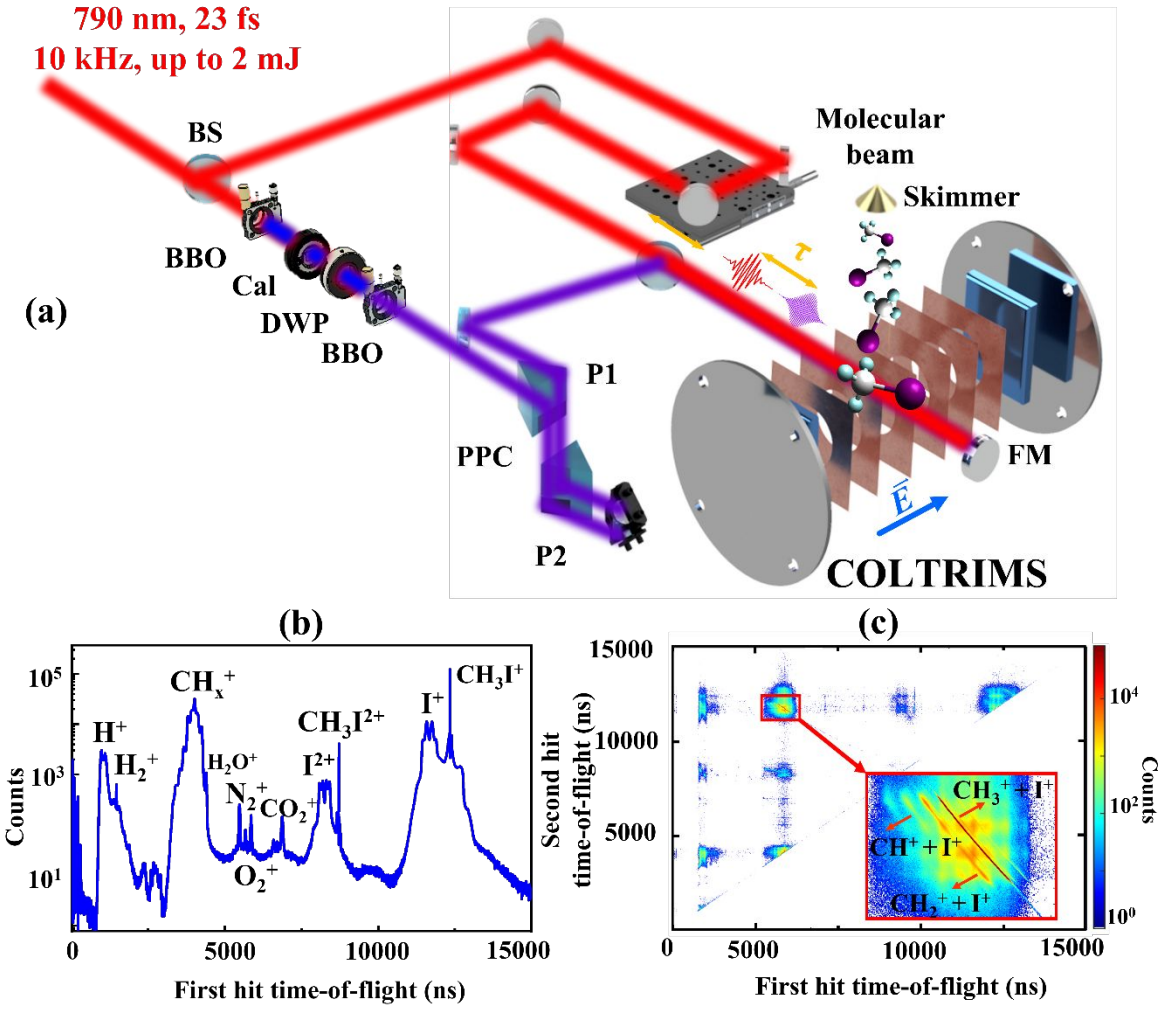

Figure 2: (a) Schematic of the experimental setup. The 263-nm and the 790-nm laser beams are collinearly propagated and focused into a supersonic beam of CH_3I molecules at the center of a COLd Target Recoil Ion Momentum Spectrometer (COLTRIMS). Ions were detected with a time- and position-sensitive detector. The electron side of the spectrometer was not used in this experiment. BS: 80:20 Beam Splitter, BBO: beta Barium Borate crystal, Cal: Calcite, DWP: Dual Wave Plate, PPC: Prism-Pair Compressor, P1: Prism #1, P2: Prism #2, FM: Focusing Mirror. τ is the variable time delay between pump

and probe pulses. (b) Delay-integrated ion time-of-flight spectrum and (c) delay-integrated PIPICO spectrum. The inset shows a zoomed view of the region containing the $CH_3^+ + I^+$ coincidences.

The UV-pump and NIR-probe beams are recombined outside the vacuum chamber containing a COLd Target Recoil-Ion Momentum Spectrometer (COLTRIMS) [56, 57, 58, 59]. An in-vacuum spherical concave mirror (f = 75 mm) focuses the copropagating laser beams onto a supersonic molecular beam at the center of the spectrometer. The molecular beam is produced by expanding the target gas into the vacuum system through a flat 30-μm diameter nozzle. Two skimmers and an adjustable slit provide collimation of the molecular beam before it reaches the spectrometer's interaction region. Ionic reaction products of the laser–molecule interaction are guided onto a time- and position-sensitive microchannel plate detector (equipped with a delay-line anode) by a weak electric field, 69.2 V/cm, applied parallel the spectrometer axis, which is also parallel to the laser polarization axis. Typical examples of TOF and photoion-photoion coincidence (PIPICO) spectra obtained in this pump-probe experiment are shown in Fig. 2(b) and Fig. 2(c), respectively. In the subsequent analysis, the ions' momenta are calculated from the time-of-flight (TOF) and impact position on the detectors [59]. The momentum conversion is verified using the well-known kinetic energy spectrum of H^+ fragments of H_2 produced by strong-field ionization [60]. False coincidence events, i.e., ion pairs originating from different molecules, are suppressed by imposing momentum conservation such that further subtraction of false coincidences is not necessary.

The NIR pulse intensity is calibrated by measuring the recoil-momentum distribution of Ne^+ ions emitted along the laser polarization following the method described in Ref. [61]. The longitudinal Ne^+ momentum distribution displays a sharp kink that mirrors a similar kink in the photoelectron spectrum of Ne at a KE of $2U_p$, where U_p is the average quiver energy of a free electron. This structure represents the transition from direct to re-scattered electrons [61]. The UV pulse intensity is estimated using Gaussian beam optics for the beam parameters and focusing geometry used in this experiment. For most of the data shown here, a NIR laser pulse energy of 6 μJ corresponding to a peak intensity of 2.8×10^{14} W/cm^2 and a UV pulse energy of 0.6 μJ corresponding to a peak intensity of 1.5×10^{13} W/cm^2 are used unless noted otherwise. At these conditions, the ion count rate from the NIR pulses alone is 4 kHz, with an almost negligible additional contribution from the UV pulses. The temporal overlap ("time zero") and the instrument response function of the UV-pump – NIR-probe setup were determined *in-situ* by

evaluating the time-dependent Ar^+ yield stemming from the two-color (UV+NIR) ionization of Ar.

3. Results and Discussion

One of the main goals of this work is to visualize the dynamics following the absorption of a single UV photon employing (time-resolved) Coulomb explosion imaging [27, 32 38, 39, 42, 41, 62-73] combined with coincident ion detection. However, at the UV-pump-pulse intensities of up to 3×10^{13} W/cm^2 used here, contributions from competing processes resulting from the absorption of two or three UV photons cannot be neglected and, therefore, need to be identified and disentangled. We probe the dynamics triggered by the UV-pump pulse by tracing delay-dependent yields and kinetic energies of the fragments produced by the intense NIR-probe pulse, restricting ourselves at present to the analysis of the final products originating from singly- or doubly-charged states of the CH_3I molecule.

The one-, two-, and three-photon excitation scenarios in our pump-probe experiment along with a set of one-dimensional cuts through the relevant PES along the C-I internuclear distance (henceforth referred to as potential energy curves (PEC) for simplicity) are illustrated in Fig. 1. These scenarios can be classified into three groups:

(1) *A*-band dissociation: Under our experimental conditions, single-photon excitation to the *A*-band of CH_3I is the dominant process induced by the pump pulse. It results in a rapid C-I bond cleavage, which leads to neutral CH_3 and I fragments, as described in the Introduction. A subsequent NIR-probe pulse singly or multiply ionizes the dissociating molecule, as sketched in Fig. 1(a) and discussed in detail in sections 3.1 and 3.4.

(2) Rydberg-state excitation: Absorption of two UV photons can excite CH_3I to high-lying Rydberg states, slightly below its ionization threshold, which is 9.54 eV [4]. Fig. 1(b) shows a schematic representation of the energy levels involved in such transitions. The two UV-photons can be absorbed simultaneously or sequentially within the duration of the pump-pulse. In the latter case, the first UV photon excites the molecule to the dissociative *A*-band manifold, and the molecule absorbs the second photon at somewhat larger C-I separation. The NIR-probe

pulse then ionizes the molecule to one of the bound or dissociating mono-cationic or di-cationic states. Signatures of this process are discussed in section 3.5.

(3) Three-photon dissociative ionization: At high UV intensities, another possible scenario is three-photon ionization by the pump pulse, as illustrated in Fig. 1(e). This process could either occur as a direct, "vertical" ionization or could involve some intermediate dynamics, in the *A*-band or in one of the high-lying Rydberg states, between the individual absorption steps, similar to scenarios (1) and (2) above. For visual clarity, only the direct ionization pathway is shown in Fig. 1(e). The ensuing dynamics can be probed by further excitation or ionization induced by the NIR-probe pulse, as described in section 3.3.

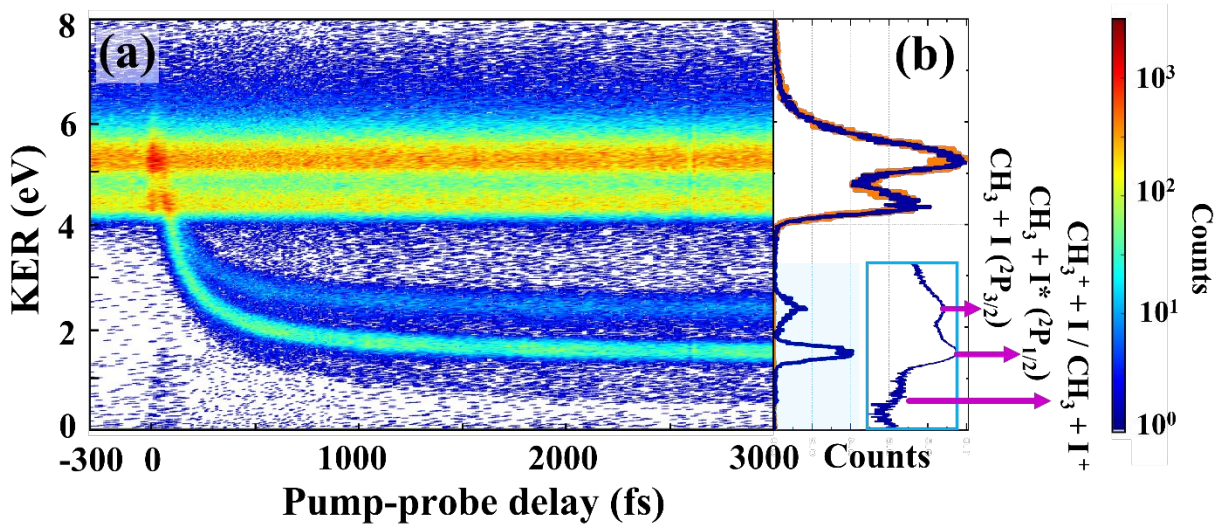

Figure 3: (a) $CH_3^+ + I^+$ coincidence yield as a function of pump-probe delay and KER. Negative and positive delays correspond to the NIR pulse arriving before and after the UV pulse, respectively. (b) Projections of the yield in the delay range of 2.5 to 3 ps (blue) and -500 to -100 fs (orange) onto the KER axis. The low-KER range of the projection is also shown on a logarithmic scale as an inset to highlight the weak contribution from dissociative ionization by the pump pulse. The three peaks in the inset are labeled according to their respective dissociation pathways, as discussed in detail in the text.

3.1 Coulomb explosion imaging of UV-induced dissociation dynamics

We start the discussion of our pump-probe experiment by analyzing spectra of coincident CH_3^+ and I^+ ion pairs resulting from molecules that are doubly charged after the probe pulse. In Fig. 3, the yield of the $CH_3^+ + I^+$ channel is plotted as a function of UV-pump – NIR-probe delay and

kinetic energy release (KER). The plot is dominated by two delay-independent horizontal bands centered at 4.4 and 5.2 eV. These bands mainly originate from molecules undergoing double ionization and fragmentation by the probe pulse alone, with minor contributions from molecules which were excited by the pump pulse but remained bound. The central KER values of these bands match the results obtained in experiments with a single NIR pulse [24] as well as earlier UV-NIR [39] and NIR-NIR [41] pump-probe experiments. According to 1D wave packet and SA-CASSCF calculations reported by Corrales *et al*. [24], the broad KER peak centered at 5.2 eV arises from several di-cationic states correlated with $I^+(^3P_{2,\,1,\,0},\ ^1D_2)$ and CH_3^+ in its ground electronic state, while the peak at 4.4 eV is correlated with $I^+(^1D_2)$ and ground-state CH_3^+.

Alongside the two delay-independent bands, we observe three delay-dependent features, which emerge from the high-energy band around zero delay and whose KER decreases as the delay increases. This decrease in KER as a function of delay is typical for the Coulomb explosion (CE) of a dissociating molecule since the resulting Coulomb repulsion is smaller the further the (neutral) dissociation products are apart by the time they are ionized by the probe pulse [42, 39]. Based on the asymptotic dissociation energies reported in literature [12], the two dominant channels are assigned to scenario 1 (i.e., CE of the ionized CH_3 and I or I* neutral fragments produced via *A*-band dissociation) in accordance with previous assignments [42, 39]. The weak delay-dependent channel observed at the lowest KER is attributed to scenario 3, i.e., three-photon dissociative ionization of CH_3I by the pump pulse. Detailed analysis of this channel is reported in Section 3.3, where the influence of multi-photon excitation processes, by the pump pulse, on the observed dynamics is discussed.

3.2 Two-color single ionization and the role of light-induced conical intersections

The same features discussed for Fig. 3 are also observed in the delay-dependent KER spectrum derived from CH_3^+ fragments alone, which are shown in Fig. 4(a). In addition to the events included in Fig. 3, this graph also contains events where the CH_3^+ fragment is produced with either a neutral partner or with a charged fragment other than I^+. All the low-KE CH_3^+ ions in Fig. 4(a) that are absent in the coincident data of Fig. 3 result from the breakup of singly charged CH_3I^+ molecules. Most of these dissociative single-ionization events are induced by either UV or NIR pulses alone (for our experimental conditions, their yield is dominated by the latter), and they show up as a delay-independent feature with a KER peaking near 0 eV.

However, there is also a clear delay-dependent feature superimposed on this delay-independent single-pulse "background". As seen in the projection onto the KER axis in Fig. 4(b), this feature, which only appears when the UV pulse precedes the NIR pulse (i.e., at positive delay values), is mostly concentrated in two peaks centered at ~1.37 eV and ~2.25 eV. These peaks are consistent with the expected KERs of

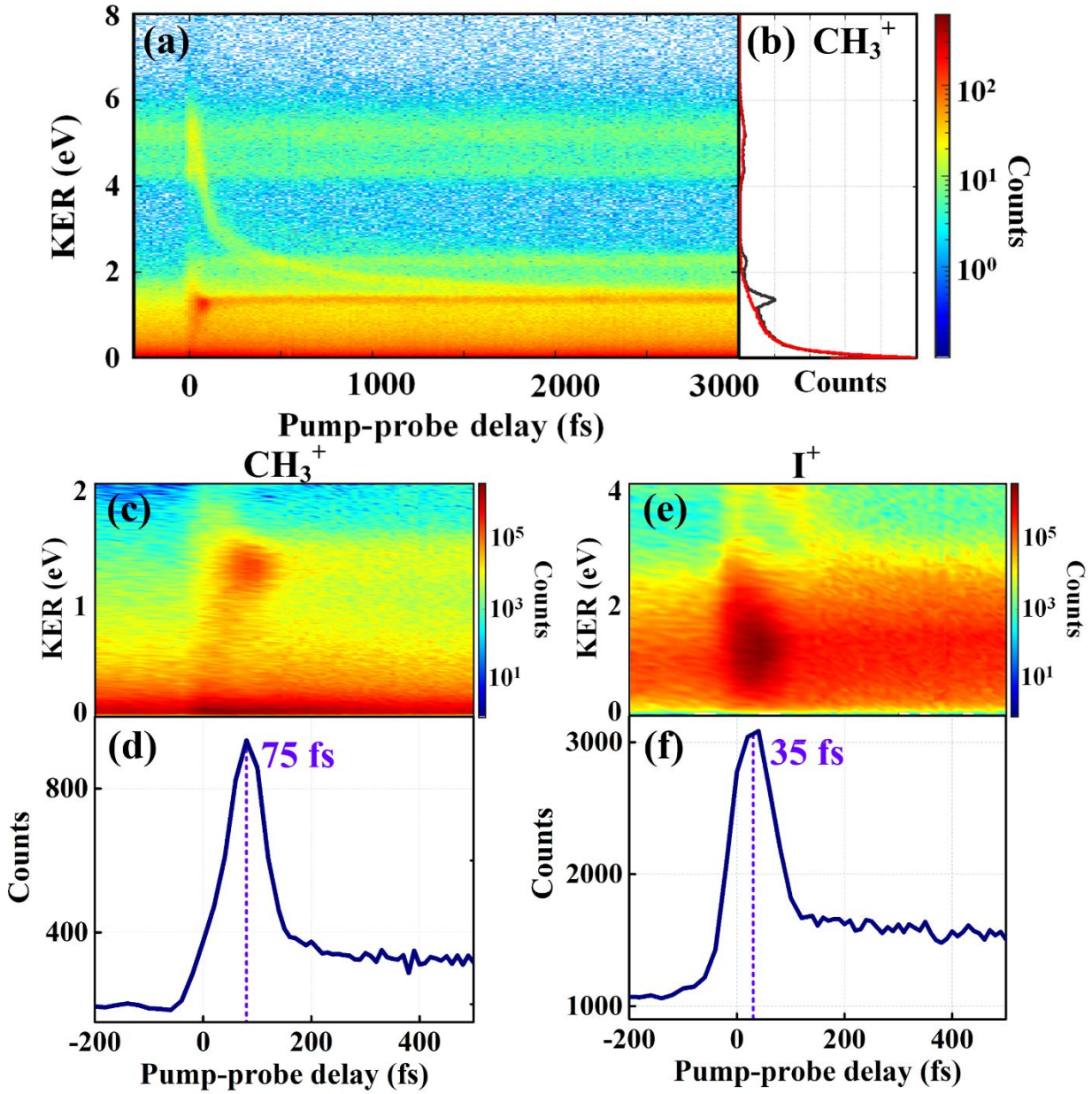

Figure 4: (a) Delay-dependent KER derived from all detected CH_3^+ ions (i.e., KER calculated from the CH_3^+ ions' KE by invoking momentum conservation with an iodine co-fragment). (b) Projection of the ion yield onto the KER axis in the delay range of 2.5 to 3 ps (black) and -300 to -100 fs (red). (c) Zoom-in on the low-KER region for delays between -200 and 500 fs. (d) Projection of the ion yield within the zoomed-in region in panel (c) onto the delay axis. (e) and (f) are the same as (c) and (d), respectively, but for all detected I^+ ions (with the KER calculated assuming a methyl co-fragment).

the CH_3 + I^* and CH_3 + I dissociation channels, respectively, reported, e.g., in earlier pump-probe experiments that did not use coincident detection [39, 42]. The corresponding ions are generated if the NIR-probe pulse arrives when the neutral molecule is already fully dissociated (i.e., at internuclear distances where the neutral PECs are flat) and therefore appear as two mostly horizontal bands in Fig. 4(a).

However, there is an additional enhancement of low-KE CH_3^+ and I^+ ions near zero delay, which can best be seen in the zoomed-in view of the low-KER region shown in Fig. 4(c) for CH_3^+ and in Fig. 4(e) for I^+ fragments, as well as the corresponding projections onto the delay axis in Fig. 4(d) and Fig. 4(f). Although an overall enhancement of the ionization yield at zero delay, driven by the simultaneous presence of both pump and probe pulses can be expected and is a common feature in pump-probe experiments [39, 18, 74], the low-KE ion yield displays a pronounced maximum at a delay of 75 fs for CH_3^+ and 35 fs for I^+. Moreover, Fig. 4(c) exhibits a feature starting from zero KE at zero delay and reaching a maximum yield at a KE of 1.25 eV at 75 fs. A similar feature was already observed in earlier pump-probe experiments by Corrales *et al.* [26, 42], where it was attributed to the creation of a light-induced conical intersection (LICI) in the neutral CH_3I by a moderately intense NIR pulse. Indeed, the $^3Q_0$ excited state is separated from the ground state by exactly one 780-nm photon at an internuclear distance of ~5.4 to 5.5 a.u., which, in the presence of the NIR pulse, results in the creation of a LICI. When crossing such a LICI, part of the wave packet, for which the KE acquired while evolving on the excited state is sufficient to overcome the remaining binding energy, can proceed to dissociation on the up-shifted ground state. This leads to the production of a CH_3 + I ($^2P_{3/2}$) fragment pair. However, because of the potential well in the CH_3I ground state, the KEs of the fragments produced via the LICI are lower than the asymptotic KEs for dissociation on the excited states. Qualitatively, the KER of the LICI channel and, thus, the KE of the resulting individual fragments can be expected to vary, ranging from 0 eV when the wave packet has just enough energy to overcome the binding energy, to the full energy of 1.37 eV corresponding to undisturbed dissociation on the excited state. This expected change of the KER as a function of delay is consistent with the tilted feature in Fig. 4(c). We note that the experiment reported by Corrales *et al.* in Ref. [26] employed a dedicated "control" NIR pulse with variable parameters to induce the LICI and a separate probe pulse at a large delay. In contrast, the single NIR pulse in our experiment *both* reshapes the PES to create the LICI *and* probes the dissociating fragments via ionization. Since

the intensity of our NIR pulse is relatively high (2.8×10^{14} W/cm^2) and since the LICI formation requires only one NIR photon, the effective time window where LICI formation is possible is much longer than the 23-fs (FWHM) duration of the NIR pulse. Therefore, the observed increase of the yield up to a delay of ~75 fs is consistent with the LICI explanation. We also note that in the other experiment by Corrales *et al.* [42], where the configuration was similar to the present study but both pulses were significantly longer, a tilted low-energy feature with a very similar shape was observed at delays up to ~100 fs.

While the above interpretation based on the LICI picture gives a reasonable explanation for the KE and the temporal dependence of the low-KE CH_3^+ feature, it does not directly account for different positions of the yield maxima in the delay-dependent CH_3^+ and I^+ features, which are clearly observed when comparing the projections in Fig. 4(d) and Fig. 4(f). A similar effect was also observed in an earlier UV-NIR pump-probe experiment by Durá *et al.* [18], where the authors considered and ruled out pure ionic- or Rydberg-state dynamics as potential scenarios behind their observations. Instead, they focused on the pathways involving the initial one-photon excitation in the *A*-band, followed by the absorption of additional UV photon(s) later in the pump pulse. In this scenario, the first UV-photon absorption initiates dissociation on the *A*-band and launches a wave packet on the repulsive excited-state manifold. While the wave packet is accelerated on these PECs before the probe pulse arrives, it can absorb further UV photon(s), e.g., from the trailing edge of the pump pulse. As sketched in Fig. 1(b), the absorption of one additional UV photon populates one of the high-lying Rydberg states slightly below the ionization threshold, which can be coupled to the ground ($\tilde{X}$) or to the first excited ($\tilde{A}$) ionic states by simultaneous or subsequent absorption of one or a few NIR photons. If the wave packet moving along the neutral PECs has already gained enough energy, it can escape the corresponding ionic potential well, thus resulting in the production of CH_3^+ or I^+ ions. Since the asymptotic limit for the production of I^+ is ~0.6 eV higher than for CH_3^+ [35, 41], the range of internuclear separations where the $I^+ + CH_3$ dissociation channel remains accessible with two UV and three NIR photons is smaller than for $I + CH_3^+$, which could cause an earlier peak of the delay-dependent I^+ yield in Fig. 4(f). In principle, the UV-intensity dependence of the ion yield in the regions of interest should allow the distinction between processes driven by one- or two-UV-photon absorption. However, this did not yield a definitive answer within the range of UV intensities available in the experiment. Based on the present data, we therefore cannot prove or

rule out either one of the two mechanisms outlined above, and it is likely that the yield at low KER contains contributions from both.

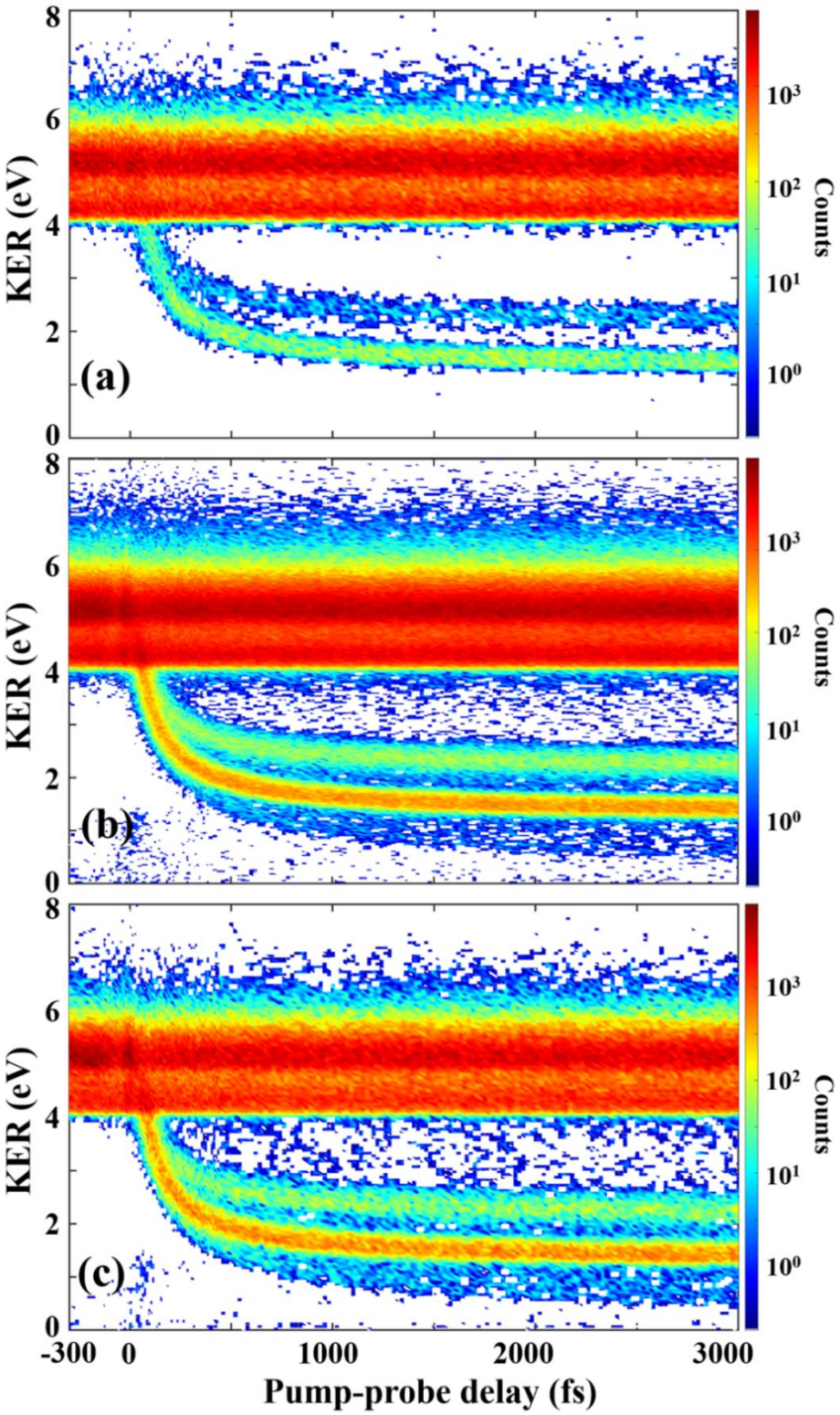

Figure 5: Delay-dependent KER of the $CH_3^+ + I^+$ channel at different UV intensities: **(a)** 1×10^{13} W/cm^2, **(b)** 2×10^{13} W/cm^2, and **(c)** 3×10^{13} W/cm^2. The NIR peak intensity is kept constant at 5×10^{14} W/cm^2 for all three cases, and all other experimental parameters are kept constant as well.

3.3 Three-photon dissociative ionization

Our discussion in Section 3.1 mentioned the presence of a weak band at a lower KER than the more intense descending KER feature in Fig. 3, and we tentatively assigned this weak feature to dissociative ionization induced by three-UV-photon absorption in the pump pulse. This process, referred to as scenario (3), is sketched in Fig. 1(c). The weak band can be observed in Fig. 3 starting from ~200 fs and reaching a KER value of ~1.3 eV at the largest delay. In the projection onto the KER axis in Fig, 3(b), this weak feature is more visible in a logarithmic-scale representation shown as an inset. To corroborate the assignment to three-photon dissociative ionization, we first verified that the UV pulse alone does indeed produce some measurable dissociative ionization yield, most notably CH_3^+ and I^+ production. Next, we investigate in Fig. 5 the dependence of the yield of this feature on the pump laser intensity to verify the non-linear dependence of the corresponding yield on the UV intensity. Figure 5 presents the delay-dependent KER for the $CH_3^+ + I^+$ channel similar to Fig. 3 but measured with three different UV-pump-pulse intensities at a fixed NIR-probe-pulse intensity. Figure 6 shows the projections of the delay-dependent maps, shown in Fig. 5, onto the KER axis for the delay range from 2.5 to 3 ps. The data are normalized to the maximum of the peak near ~1.5 eV, which is due to single UV photoabsorption, and thus is expected to scale linearly with UV intensity. As expected, the second single-photon channel at ~2.3 eV has the identical intensity dependence. At the same time, the low-KER feature between 0.5 and 1 eV clearly manifests a steeper, non-linear dependence on the UV pulse intensity, confirming that it originates from a multi-photon process.

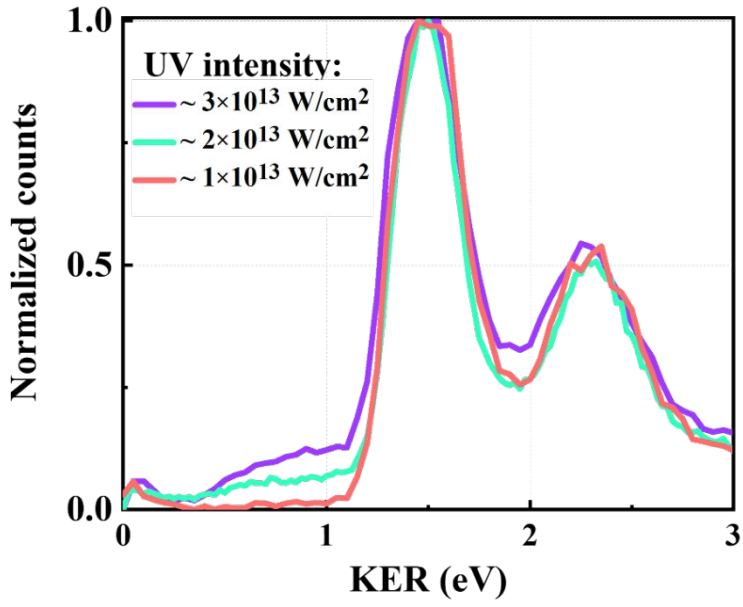

Figure 6: Projections of the $CH_3^+ + I^+$ coincidence yield shown in Fig. 5, integrated over the delay range from 2.5 to 3 ps, onto the KER axis for the three UV intensities. The maximum of

each spectrum is normalized to one. Note that the small peak close to zero is due to remaining false coincidences.

At a central wavelength of 263 nm, absorption of three UV photons deposits a total energy of 14.1 eV in the molecule, which is well above the asymptotic dissociation limits for several low-lying dissociating states of CH_3I^+, as shown in Fig. 1(c). However, while this energy is sufficient to populate the high-lying vibrational levels of the Ã state of CH_3I^+, it is insufficient to directly reach any of the higher-lying repulsive ionic B̃ states by a vertical transition. Although it is known that the CH_3I^+ Ã-state's vibrational levels above $\upsilon = 10$ dissociate by internal conversion to the $\tilde{X}$ state (converging to the asymptotic $CH_3^+ + I$ ($^2P_{3/2}$) limit), this process proceeds on a time scale of nanoseconds [75, 76]. Therefore, the Ã state remains bound on the few-ps time scale of our experiment. Ionization to the Ã state also does not produce I^+ ions, which are clearly present in our UV-only spectra. Therefore, our experimental observations suggest that the three-photon dissociative ionization by the UV-pump pulse proceeds via the direct population of one of the

repulsive ionic states. In a "vertical ionization" scenario, this could be realized by absorbing more energetic UV photons from the blue spectral edge of the UV pulse. However, more likely, such a transition is facilitated by intermediate dynamics upon the absorption of the first one or two UV photons, which in turn reduces the energy needed for ionization due to stretching of the C–I bond. A CE simulation confirming the assignment of this feature in the delay-dependent KER maps is presented in the next section.

3.4 Coulomb explosion simulations

To simulate the pump-probe experiments described here, the KER of an ion pair produced by the probe pulse at a time delay, t, between the pump and the probe pulses is calculated as the sum of the translational energy, E_{trans}, that both fragments gained during the photodissociation induced by the pump pulse, and the energy of the Coulomb repulsion, E_{CE}, between the two ions following double ionization:

$$\mathbf{KER}(\boldsymbol{t}) = \boldsymbol{E}_{\mathbf{trans}}(\boldsymbol{t}) + \boldsymbol{E}_{\mathbf{CE}}(\boldsymbol{t}) \,. \qquad (1)$$

Assuming a purely Coulombic di-cationic PEC, the value of E_{CE} can be calculated using the Coulomb energy of two point charges separated by the C-I internuclear distance, R, at time t.

E_{trans} can be determined from the PECs of the $^3Q_0$ and $^1Q_1$ electronic states underlying the CH_3I *A*-band taken from Alekseyev *et al.* [14]. From those, the relative velocity, $v(R)$, of the dissociated fragments can also be computed via a one-dimensional classical model assuming zero initial velocity:

$$v(R) = \sqrt{2\frac{U(R_0) - U(R)}{\mu}}\,. \qquad (2)$$

Here, R_0 is the equilibrium internuclear distance (2.18 Å), *U(R)* is the potential energy of the excited state, and μ is the reduced mass for the CH_3–I two-body system. The time-dependent changes in the C-I internuclear distance, *R(t),* during the dissociation can then be obtained by solving the equation:

$$t = \int_{R_0}^{R(t)} \frac{dR}{\sqrt{\frac{2}{\mu}[U(R(t)) - U(R_0)]}}\,. \qquad (3)$$

Based on the known photoabsorption cross sections [13], we make the simplifying assumption that the photoexcitation at 263 nm exclusively populates the $^3Q_0$ state and that the $^1Q_1$ state is populated only through a transition enabled by the conical intersection between the two excited states. To simulate the dynamics on the $^1Q_1$ state, we therefore calculate the propagation time of the classical two-body system on the $^3Q_0$ state to reach the conical intersection at a C-I distance of 2.37 Å (which is found to be approximately 9.17 fs), and then proceed with the propagation using the $^1Q_1$ state PEC. The resulting time-dependent velocities and internuclear distances for the dynamics evolving on the $^3Q_0$ and $^1Q_1$ states are presented in Fig. 7. They display the expected monotonic increase in C-I internuclear distance and illustrate how the velocity increases from zero to an asymptotic value within approximately 50 fs, corresponding to a distance

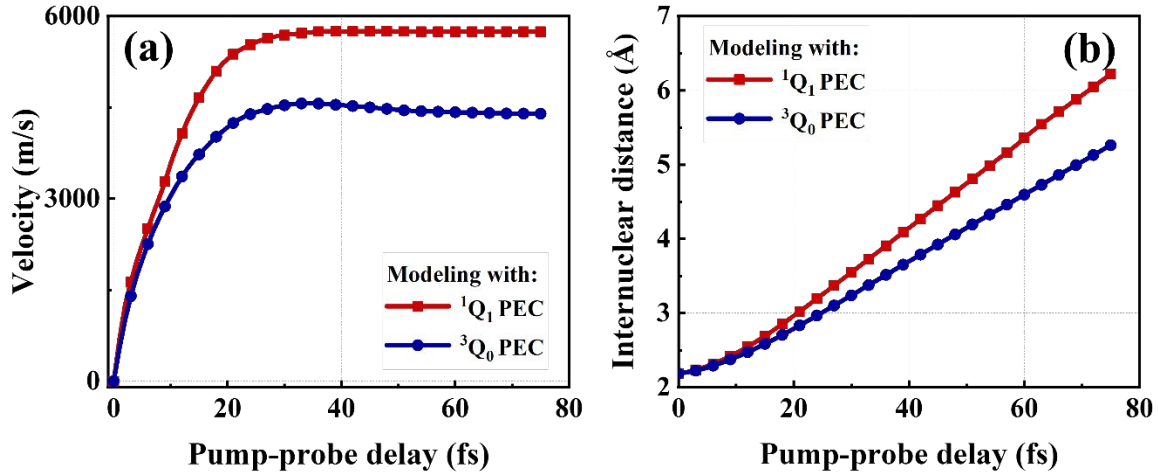

Figure 7: Time-dependence of the (a) relative CH_3–I velocity and (b) C-I internuclear distance determined for the dissociative PECs of the $^3Q_0$ and $^1Q_1$ states reported by Alekseyev et al. [14]. The steeper slope of the $^1Q_1$ state results in a larger acceleration and thus a higher final velocity.

of about 10 Å. Variations in the final velocities associated with the shape of the $^3Q_0$ and $^1Q_1$ states are also apparent, where the steeper gradients on the $^1Q_1$ PEC result in a higher final velocity. To test how sensitive the simulations are to the detailed shape of the PEC, a comparison of these results with the predictions of two simplified models often used in literature, which either assume that the dissociating fragments travel with constant velocities [27, 32, 38, 39] or that the velocity rises exponentially towards its asymptotic value [74], is shown in the ESI.

The simulated KER for dissociation along both the $^3Q_0$ and $^1Q_1$ states is presented in Fig. 8(a) along with the experimental data. The simulations agree with the experimental KERs at large delays (or internuclear distances), but a discernible mismatch is observed within the first ~100 fs, where the KER is clearly overestimated by the model calculations. This mismatch highlights the fact that the simplified treatment of the di-cationic PECs as purely Coulombic is not appropriate for small internuclear distances (see Fig. 1). This is to be expected (see, e.g., Schouder *et al*. [77]) and also supported by the calculations reported by Corrales *et al.* [24], which even predict the existence of potential barriers in the Franck-Condon region for various PECs associated with low-lying electronic states of CH_3I^{2+} correlating with the $CH_3^+ + I^+$

asymptote. We therefore improve our model by utilizing the di-cationic PECs reported by Corrales *et al.* [24], which modifies Equation (1) to:

$$\mathrm{KER}(t) = E_{\mathrm{trans}}(t) + E_{\mathrm{CE}}(t) + E_{\mathrm{corr}}(R(t)) = \frac{1}{2}\mu v^2(t) + \frac{k q_{\mathrm{CH3}} q_I}{R(t)} + E_{\mathrm{corr}}(R(t)) \,, \qquad (4)$$

where *v(t)* is the time-dependent relative velocity, *k* is the Coulomb constant, q_{CH3} and q_{I} are the charges on the methyl and iodine fragments, and *R* is the time-dependent C-I distance. E_{corr} is a correction term accounting for deviations from a purely Coulombic interaction on the di-cation PECs taken from Corrales *et al*. [24]. The resulting simulated KER is presented in Fig. 8(b) and shows a much better agreement with the experimental observations. In particular, the simulations show an initial *increase* of the KER at small delays, which results from the shape of the potential well in the di-cationic PECs. Clearly, the significantly improved time resolution of our experiment compared to previous studies [18, 24, 42] is beneficial for resolving this experimental signature of the CH_3I^{2+} potential well, which is visible in the first hundred femtoseconds, as highlighted in the inset in Fig. 8(b).

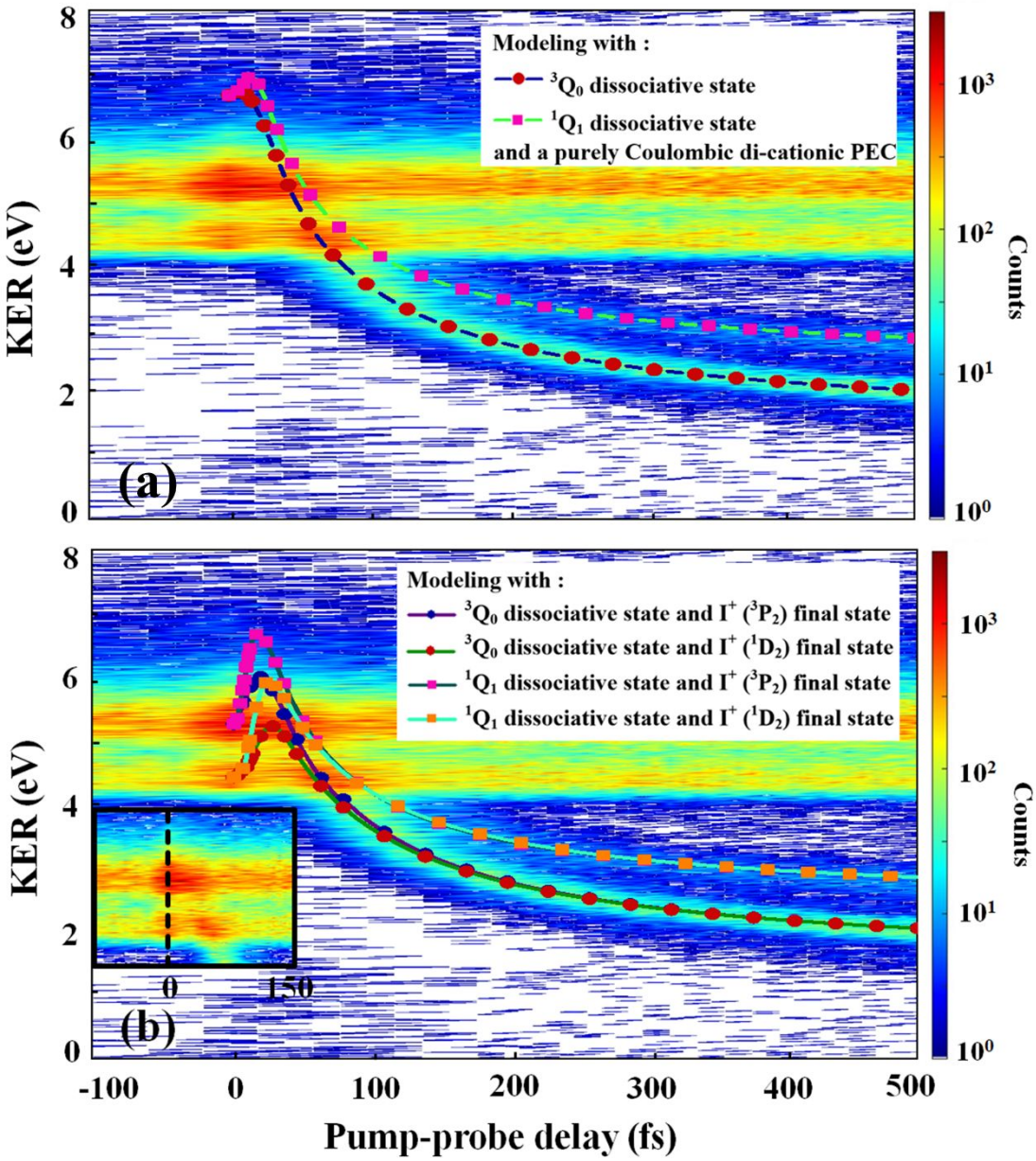

Figure 8: Comparison of the Coulomb explosion simulations for both the $^3Q_0$ and $^1Q_1$ states with the experimental delay-dependent KER of the $CH_3^+ + I^+$ channel. The experimental data is the same as shown in Fig. 3. (a) Simulations assuming a purely Coulombic di-cationic final state. (b) Simulations using the di-cationic PECs from Corrales et al. [24]. The specific di-cationic PEC correlated with different I^+ states used for each simulation are indicated in the figure. In both (a) and (b), the dissociation dynamics on the $^3Q_0$ and $^1Q_1$ states are modeled using the PECs from Alekseyev et al. [14]. For better visibility, the inset in (b) shows the region near zero delay without the model curves.

We note that because of the potential well, dissociation and CE at small pump-probe delays are classically allowed only if the KE of the two-body system (e.g., gained on the neutral dissociative PEC) is greater than the height of the potential barrier, otherwise the molecule remains bound and will be detected as a metastable CH_3I^{2+}. Our calculations show that the system needs to propagate for approximately 13 fs, or ~ 0.3 Å, on the neutral PEC, to gain the required energy to overcome the potential barrier in the lowest di-cationic state. Indeed, the delay-dependent yield of CH_3I^{2+} (see Fig. S3 in the ESI) shows a small enhancement when the pump and probe pulses overlap in time, but the temporal resolution is not sufficient to extract further information.

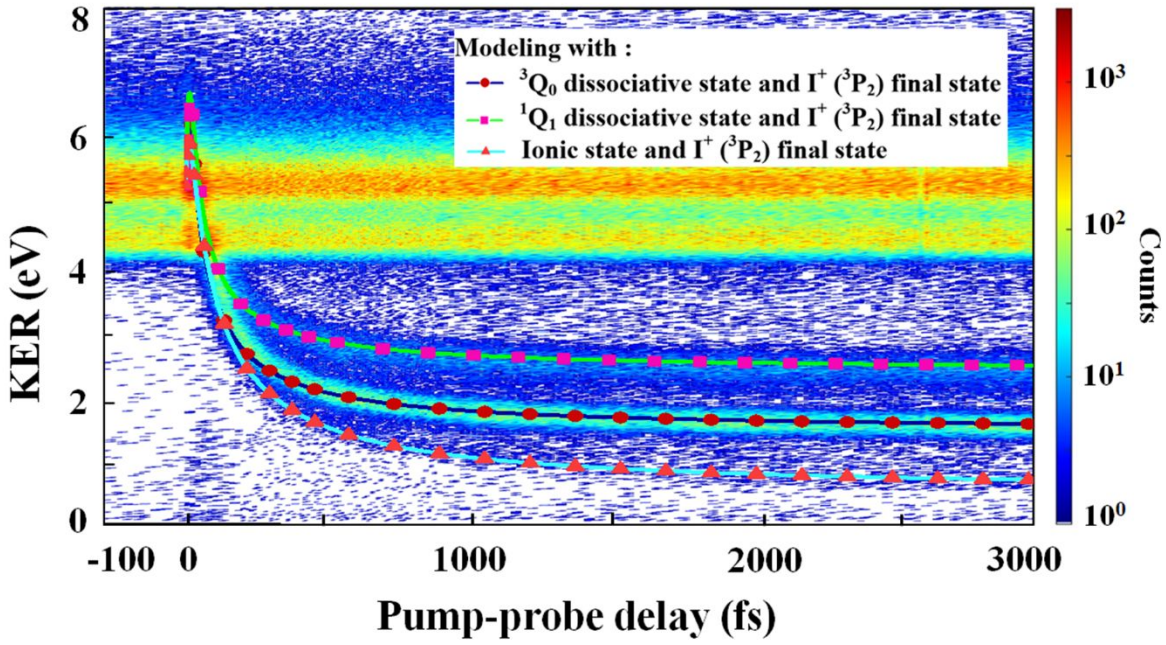

Figure 9: Comparison of the experimental delay-dependent KER of the CH_3^++I^+ channel shown in Fig. 3 with Coulomb explosion simulations assuming excitation by the pump pulse to the $^3Q_0$ or $^1Q_1$ states or to a dissociative mono-cationic state, followed by ionization by the probe pulse to the di-cationic CH_3^++I^+ ($^3P_2$) state. For modeling the dynamics on the neutral excited states, the PECs from Alekseyev et al. [14] were used, while the dynamics on the dissociative mono-cationic state were modeled using an exponentially rising dissociation velocity (see text). The di-cationic final state was modeled using the PEC for the CH_3^++I^+ ($^3P_2$) state from Corrales et al. [24].

Finally, we also performed CE modeling for the dissociative ionization channel that appeared as the lowest time-dependent KER feature in Fig. 3. Since the exact mono-cationic

PEC involved in this process is unknown, we simulate the dynamics in the mono-cation using an exponentially rising dissociation velocity together with an asymptotic KER value of 0.4 eV obtained from the experimental data measured at large delays. To simulate the Coulomb explosion, we employ the lowest di-cationic PEC, $CH_3^+ + I^+ (^3P_2)$. The results are in good match with the experimental data, as shown in Fig. 9.

3.5 Two-photon Rydberg-state excitation

The dynamics induced by excitation to Rydberg states of CH_3I have been investigated experimentally [10, 19, 23, 30, 45, 46] and theoretically [22]. Excitation of low-lying Rydberg states at wavelengths near 200 nm corresponds to a transition to bound states followed by predissociation through crossings between the bound Rydberg states ($^3R_{0,1,2}$, ^1R) and the steep repulsive components of the $^3A_1$ valence state, which converges to the same atomic limit as the $^3Q_0$ dissociative state, i.e., $CH_3 + I^*(^2P_{1/2})$ [22]. Excitation to the manifold's higher-lying states right below the ionization threshold yields atomic iodine Rydberg states [8] and ground-state methyl fragments.

When using a femtosecond laser pulse to excite CH_3I to the *A*-band by one-photon absorption, it can be difficult to avoid populating several higher-lying Rydberg states by two-photon absorption processes, either directly or in a stepwise manner via the intermediate *A*-band. To investigate this competition between one-photon excitation to the *A*-band and multi-photon excitation by the pump pulse to the high-lying Rydberg states of CH_3I, we turn to the intensity and delay dependence of the CH_3I^+ yield. Figure 10 presents the CH_3I^+ yield for the same set of pump-pulse intensities as in Sec. 3.3 and at a fixed NIR peak intensity of 5×10^{14} W/cm^2. This yield exhibits a pronounced enhancement when the UV and NIR pulses overlap in time, which is Gaussian in shape for the smallest pump intensity and becomes asymmetric at higher intensities with a pronounced tail, "exponential decay", gradually developing at positive delays. The temporal profiles of this yield suggest that at the lowest UV intensity (1×10^{13} W/cm^2), the enhancement is due to non-sequential two-color ionization of the molecule, which reflects the cross-correlation of the two pulses. As the intensity is increased from 1×10^{13} to 3×10^{13} W/cm^2, an additional, exponential decay, contribution to the CH_3I^+ yield appears, which we interpret as a signature of Rydberg states that are populated by two UV-photon excitations, as sketched in Fig. 1(b).

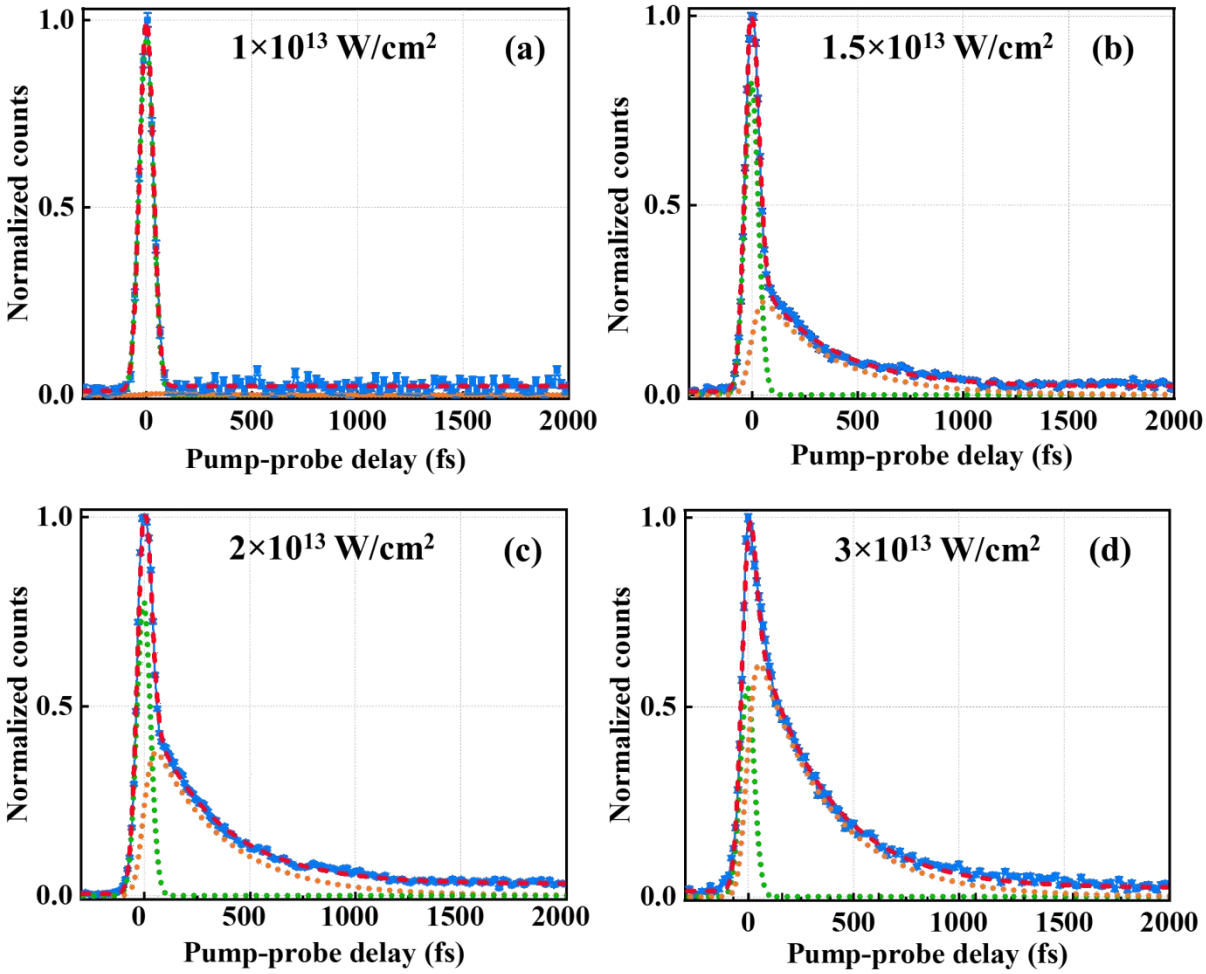

Figure 10: (a-d) Delay-dependent yield of CH_3I^+ for different UV intensities (indicated in each panel), with the maximum of each trace normalized to one. The intensity of the NIR probe pulse is kept constant at 5×10^{14} W/cm^2. Least-square fits of the function given in Eq. 5 are shown as dashed red lines, while each of the components of this fit function (Gaussian: green; exponential: orange) are included as dotted lines. The fit parameters are given in Table 1.

Consequently, at small pump-probe delays where UV and NIR pulses overlap in time, there would be competition between the two processes: (1) single UV photoexcitation followed by the NIR vertical ionization in the Franck-Condon region, and (2) two-photon UV excitation to the Rydberg state series with subsequent single-photon ionization by the NIR. The resulting delay-dependent yield transforms from a Gaussian distribution at the lowest intensity in Fig. 10(a), which is mainly due to the instrument response, to a Gaussian with an exponential-decay tail extending to longer delays at higher intensities. To characterize these two processes more

quantitatively, the time-dependent CH_3I^+ yield in Fig. 10 were fitted by the sum of a Gaussian function to describe process (1), which essentially mimics the cross-correlation between the two pulses; and an exponential-decay function (convolved with a Gaussian distribution of the same width to account for the instrument response function) to describe the contribution from intermediate Rydberg states with a finite lifetime, explicitly given by:

$$y(t) = \mathrm{A}e^{-\left(\frac{t-t_0}{2\sigma}\right)2} + \mathrm{B}\, e^{\frac{1}{2}\left(\frac{\sigma}{\tau}\right)^2 - \frac{(t-t0)}{\tau}}\left[\frac{1}{2}\left(erf\left(\frac{\frac{t-t0}{\sigma}-\frac{\sigma}{\tau}}{\sqrt{2}}\right)+1\right)\right] + \mathrm{C}\,. \qquad (5)$$

Here, σ is the standard deviation of the Gaussian distribution, τ is the lifetime of the exponential decay, t_0 accounts for a possible small offset from the nominal zero delay time, and a constant C is added to fit the baseline. The coefficients A and B represent the weighting factors of one-photon excitation (Gaussian) and two-photon excitation (exponential decay), respectively. The results of the least-square fit of this function to the experimental data are shown in Fig. 10, and the corresponding fit parameters are summarized in Table 1. As expected, the fits indicate a significant increase of the contribution from two-photon excitation with increasing UV intensity and yield an average value of τ =335 fs, which can be interpreted as the average lifetime of the contributing Rydberg state(s). Given the central wavelength of our UV pulses, two-UV photon excitation with a total photon energy of 9.41 eV can reach high-lying Rydberg states with 10d, 11d, and 12d character [7, 8, 13], which converge to the first ionization potential ($^2E_{3/2}$) at 9.540 eV, and/or the 8s and 6d states converging to the second ionization potential ($^2E_{1/2}$) at 10.168 eV.

Intensity (W/cm^2)	**A**	**B**	**τ (fs)**	**t_0 (fs)**
1×10^{13}	0.98 ± 0.01	0.01 ± 0.005	NA	-2.5 ± 0.5
1.5×10^{13}	0.830 ± 0.007	0.310 ± 0.005	339 ± 3	-3.9 ± 0.3
2×10^{13}	0.785 ± 0.007	0.471 ± 0.005	336 ± 4	-4.1 ± 0.3
3×10^{13}	0.55 ± 0.01	0.76 ± 0.01	330 ± 1	-8.1 ± 0.6

Table 1: Parameters extracted from fitting Eq. (5) to the time-dependent CH_3I^+ yield, shown in Fig. 10, for different UV intensities. A value of σ = (32.6 ± 0.4) fs, representing the instrument response, was obtained from the fit to the lowest-intensity data and then used as a fixed parameter for fitting the data at higher intensity.

4. Conclusion

We have studied the photodissociation dynamics of iodomethane using a UV-pump – NIR-probe scheme coupled with coincidence ion momentum imaging. Combining the analysis of coincident and non-coincident ion yields, we disentangled signatures of one-, two-, and three-UV-photon processes induced by the pump pulse and mapped the main dissociation pathways using Coulomb explosion imaging. Classical Coulomb explosion simulations are in good agreement with the experimental data and help identify the experimental signature of the potential energy well in the lowest di-cation states near the CH_3I equilibrium geometry.

In addition to the well-known dissociation of the neutral CH_3I molecule following single UV-photon excitation, two-photon excitation to high-lying Rydberg states with an average lifetime of 335 fs, and three-photon ionization to dissociative mono-cationic states were identified. The findings highlight the ability of time-resolved coincidence ion momentum imaging to disentangle competing molecular processes and reaction pathways on ultrafast timescales.

Conflicts of Interest

There are no conflicts of interest to declare.

Author Contributions

FZ, AR, and DR conceived the experiment, which was performed by FZ, KB, RF, KRP, YM, and BK under the guidance of AR and DR. FZ designed and built the setup for generating short UV pulses with help from KB, RF, KRP, YM, and TS. FZ analyzed the data with help from TS and IBI and under the supervision of AR and DR. FZ, AR, RF, IBI, and DR wrote the manuscript with input from all co-authors.

Acknowledgements

This work was supported by the Chemical Sciences, Geosciences, and Biosciences Division, Office of Basic Energy Sciences, Office of Science, US Department of Energy under grant no. DE-FG02-86ER13491. R.F. acknowledges support from the Linac Coherent Light Source,

SLAC National Accelerator Laboratory, which is supported by the same agency under contract no. DE-AC02-76SF00515.

References

[1] Kasper JVV and Pimentel GC. Appl. Phys. Lett. 1964;5:231.

[2] Riley SJ and Wilson KR. Faraday Discuss. Chem. Soc. 1972;53:132–146.

[3] Gedanken A, Rowe MD. Chem. Phys. Lett. 1975;34:39–43.

[4] Karlsson L, Jadrny R, Mattsson L, Chau FT, Siegbahn K. Phys Scr 1977;16:225–34.

[5] Parker DH, Pandolfi R, Stannard PR, and El-Sayed MA. Chem. Phys. 1980; 45:27–37.

[6] Chandler DW and Houston PL. J. Chem. Phys. 1987;87:1445.

[7] Dobber MR, Buma WJ, De Lange CA. J Chem Phys 1993;99:836.

[8] Janssen MHM, Dantus M, Guo H, Zewail AH. Chem. Phys. Lett. 1993;214:281–9.

[9] Amatatsu Y, Yabushita S, and Morokuma K. J. Chem. Phys. 1996;104:9783.

[10] Baronavski AP, Owrutsky JC. J Chem Phys 1998;108:3445–52.

[11] Eppink ATJB and Parker DH. J Chem Phys 1998;109:4758.

[12] Eppink ATJB and Parker DH. J Chem Phys 1999;110:832.

[13] Eden S, Limão-Vieira P, Hoffmann S V., Mason NJ. Chem Phys 2007;331:232–44.

[14] Alekseyev AB, Liebermann H-P, Buenker RJ, Yurchenko SN. J Chem Phys 2007;126:234102.

[15] Alekseyev AB, Liebermann HP, Buenker RJ. J Chem Phys 2007;126:234103.

[16] De Nalda R, Izquierdo JG, Durá J, Bañares L. J Chem Phys 2007;126:021101.

[17] De Nalda R, Durá J, García-Vela A, Izquierdo JG, González-Vázquez J, Bañares LJ Chem Phys 2008;128:244309.

[18] Durá J, De Nalda R, Amaral GA, Bañares L. J Chem Phys 2009;131:134311.

[19] Wang Y, Shen H, Hua L, Hu C, Zhang B. Opt Express 2009;17:10506–13.

[20] Rubio-Lago L, García-Vela A, Arregui A, Amaral GA, Banares L. J Chem Phys 2009;131:174309.

[21] González MG, Rodríguez JD, Rubio-Lago L, García-Vela A, Bañares L. Phys Chem Chem Phys 2011;13:16404–15.

[22] Alekseyev AB, Liebermann HP, Buenker RJ. J Chem Phys 2011;134:044303.

[23] Gitzinger G, Corrales ME, Loriot V, De Nalda R, Bañares L. J Chem Phys 2012;136:074303.

[24] Corrales ME, Gitzinger G, González-Vázquez J, Loriot V, De Nalda R, Bañares L. J Phys Chem A 2012;116:2669–2677.

[25] Corrales ME, Loriot V, Balerdi G, González-Vázquez J, De Nalda R, Bañares L, *et al.* Phys Chem Chem Phys 2014;16:8812–8.

[26] Corrales ME, González-Vázquez J, Balerdi G, Solá IR, De Nalda R, Bañares L. Nat Chem 2014;6:785–790.

[27] Erk B, Boll R, Trippel S, Anielski D, Foucar L, Rudek B*, et al.* Science 2014;345:288–91.

[28] Motomura K et al., J. Phys. Chem. Lett. 2015;6;2944.

[29] Attar AR, Bhattacherjee A, Leone SR. J Phys Chem Lett 2015;6:5072–5077.

[30] Xu H, Pratt ST. J Phys Chem A 2015;119:7548–58.

[31] Drescher L, Galbraith MCE, Reitsma G, Dura J, Zhavoronskov N, Patchkovskii S, Vrakking MJJ, and Mikosch J. J. Chem. Phys. 2016;145:011101.

[32] Boll R, Erk B, Coffee R, Trippel S, Kierspel T, Bomme C, *et al.* Struct Dyn 2016;3:043207.

[33] Das S, Sharma P, and Vatsa RK. J. Photochem. and Photobio. C: Photochem. Rev. 2017;33: 27–53.

[34] Poullain SM, Chicharro DV, Rubio-Lago L, García-Vela A, Bañares L. Philos Trans R Soc A Math Phys Eng Sci 2017;375:20160205.

[35] Poullain SM, Chicharro DV, González-Vázquez J, Rubio-Lago L, Bañares L. Phys Chem Chem Phys 2017;19:7886–96.

[36] Rudenko A *et al.,* Nature 2017;546:129.

[37] Baumann A, Rompotis D, Schepp O, Wieland M, Drescher M. J Phys Chem A 2018;122:4779–4784.

[38] Amini K, Savelyev E, Brauße F, Berrah N, Bomme C, Brouard M *et al.* Struct Dyn 2018;5:014301.

[39] Allum F, Burt M, Amini K, Boll R, Köckert H, Olshin PK, *et al.* J Chem Phys 2018;149:204313.

[40] Brauβe F, Goldsztejn G, Amini K, Boll R, Bari S, Bomme C, Brouard M, Burt M, Cunha de Miranda B, Düsterer S *et al.* Phys. Rev. A 2018;97:043429.

[41] Malakar Y, Pearson WL, Zohrabi M, Kaderiya B, Kanaka Raju P, Ziaee F, *et al.,* Phys Chem Chem Phys 2019;21:14090–102.

[42] Corrales ME, González-Vázquez J, De Nalda R, Banares L. J Phys Chem Lett 2019;10:138–43.

[43] Warne EM, Downes-Ward B, Woodhouse J, Parkes MA, Bellshaw D, Springate E *et al.* Phys Chem Chem Phys 2019;21:11142–9.

[44] Warne EM, Downes-Ward B, Woodhouse J, Parkes MA, Springate E, Pearcy PAJ, *et al.* Phys Chem Chem Phys 2020;22:25695–703.

[45] Matthíasson K, Koumarianou G, Jiang MX, Glodic P, Samartzis PC, Kvaran Á. Phys Chem Chem Phys 2020;22:4984-4992.

[46] Forbes R, Allum F, Bari S, Boll R, Borne K, Brouard M, et al. J Phys B: At Mol Opt Phys 2020;53:224001.

[47] Downes-Ward B, Warne EM, Woodhouse J, Parkes MA, Springate E, Pearcy PAJ, et al. J Phys B: At Mol Opt Phys 2021;54:134003.

[48] Chang KF, Wang H, Poullain SM, Prendergast D, Neumark DM, Leone SR. J Chem Phys 2021;154:234301.

[49] Li X *et al.* Phys. Rev. Lett. 2021;127: 093202.

[50] Li X *et al.* Phys Rev. Res. 2022; 4:013029.

[51] Rasmussen RA, Khalil MAK, Gunawardena R, Hoyt SD. J. Geophys. Res. Oceans 1982;87:3086–3090

[52] Tegtmeier S, Krüger K, Quack B, Atlas E, Blake DR, Boenisch H, Engel A, Hepach H, Hossaini R, Navarro MA, Raimund S, Sala S, Shi Q, Ziska F. Atmos. Chem. Phys. 2013;13:11869–11886

[53] Mulliken RS. J Chem Phys 1940;8:382.

[54] Mulliken RS, Teller E. Phys Rev 1942;61:283.

[55] Ziaee F, Borne K, Kanaka Raju P, Forbes R, Malakar Y, Kaderiya B, Severt T, Carnes KD, Ben-Itzhak I, Rudenko A, and Rolles D. Frontiers in Optics + Laser Science APS/DLS, OSA Technical Digest (Optica Publishing Group, 2019), paper FM1F.3.

[56] Ullrich J, Moshammer R, Dörner R, Jagutzki O, Mergel V, Schmidt-Böcking H, *et al.* J Phys B: At Mol Opt Phys 1997;30:2917–74.

[57] Dörner R, Mergel V, Jagutzki O, Spielberger L, Ullrich J, Moshammer R, *et al.* Phys Rep 2000;330:95–192.

[58] Ullrich J, Moshammer R, Dorn A, Dörner R, Schmidt LPH, Schmidt-Böcking H. Reports Prog Phys 2003;66:1463.

[59] Maharjan CM. Momentum imaging studies of electron and ion dynamics in a strong laser field. PhD thesis, Kansas State University, 2007.

[60] Rudenko A, Feuerstein B, Zrost K, De Jesus VLB, Ergler T, Dimopoulou C, *et al.*, J Phys B: At Mol Opt Phys 2005;38:487.

[61] Rudenko A, Zrost K, Schröter CD, Jesus VLB de, Feuerstein B, Moshammer R, et al. J Phys B: At Mol Opt Phys 2004;37:L407–13.

[62] Vager Z, Naaman R, Kanter EP. Science 1989;244:426–31.

[63] Stapelfeldt H, Constant E, Sakai H, Corkum PB. Phys Rev A 1998;58:426–33.

[64] Sanderson JH, El-Zein A, Bryan WA, Newell WR, Langley AJ, Taday PF, Phys. Rev. A 1999;59:R2567

[65] Ergler Th, Rudenko A, Feuerstein B, Zrost K, Schröter CD, Moshammer R, and Ullrich J. Phys. Rev. Lett. 2005;95:093001.

[66] Ergler T, Rudenko A, Feuerstein B, Zrost K, Schröter CD, Moshammer R, Ullrich, J. Phys Rev

Lett 2006;97:193001.

[67] Hishikawa A, Matsuda A, Fushitani M, Takahashi EJ. Phys Rev Lett 2007;99:258302.

[68] Gagnon J, Lee KF, Rayner DM, Corkum PB, Bhardwaj VR. J Phys B: At Mol Opt Phys 2008;41:215104.

[69] Bocharova IA, Alnaser AS, Thumm U, Niederhausen T, Ray D, Cocke CL, Litvinyuk, IV. Phys. Rev. A 2011; 83:013417.

[70] Pitzer M, Kunitski M, Johnson AS, Jahnke T, Sann H, Sturm F, et al. Science 2013;341:1096–100.

[71] Ibrahim H, Wales B, Beaulieu S, Schmidt BE, Thiré N, Fowe EP, *et al.* Nat Commun 2014;5:4422.

[72] Kling NG, Díaz-Tendero S, Obaid R, Disla MR, Xiong H, Sundberg M, *et al*. Nat Commun 2019;10:2813.

[73] Schouder CA, Chatterley AS, Pickering JD, and Stapelfeldt H. Annu. Rev. Phys. Chem. 2022;73:323-347.

[74] Burt M, Boll R, Lee JWL, Amini K, Köckert H, Vallance C, *et al*. Phys Rev A 2017;96:043415.

[75] Tadjeddine M, Flament JP, Teichteil C. Chem Phys 1987;118:45–55.

[76] Walter K, Weinkauf R, Boesl U, Schlag EW. J Chem Phys 1988;89:1914.

[77] Schouder CA, Chatterley AS, Madsen, LB, Jensen, F, and Stapelfeldt H. Phys. Rev. A 2020;102:063125